Journal of Aeronautics & Aerospace Engineering
ISSN: 2168-9792

Kis et al., J Aeronaut Aerospace Eng 2016, 5:2
DOI: 10.4172/2168-9792.1000164

Research Article Open Access

Determination of the Earth's Magnetic Field Gradients from Satellites Measurements and Their Inversion over the Kursk Magnetic Anomaly

Kis KI[1], Taylor PT[2*] and Wittmann G[3]

[1]Geophysics and Space Sciences Department, Loránd Eötvös University, 1117 Budapest Pázmány Péter Sétány 1/c. Hungary
[2]Planetary Geodynamics Laboratory, NASA/GSFC, Greenbelt, MD 20771, USA
[3]MOL Hungarian Gas and Oil Company, 1117 Budapest, Október Huszonharmadika u. 18. Hungary

Abstract

We computed magnetic field gradients at satellite altitude, over Europe with emphasis on the Kursk Magnetic Anomaly (KMA). They were calculated using the CHAMP satellite total magnetic anomalies. Our computations were done to determine how the magnetic field observations data from the new ESA/Swarm satellites could be utilized to determine the structure of the magnetization of the Earth's crust, especially in the region of the KMA. Ten years of CHAMP data were used to simulate the Swarm data. An initial east magnetic anomaly gradient map of Europe was computed and subsequently the North, East and Vertical magnetic gradients for the KMA region were calculated. The vertical gradient of the KMA was also determined using Hilbert transforms. Inversion of the total KMA was derived using Simplex and Simulated Annealing algorithms. The depths of the upper and lower boundaries are calculated downward from the 324 km elevation of the satellite. Our resulting inversion depth model is a horizontal quadrangle. The maximum errors are determined by the model parameter errors.

Keywords: Earth's magnetic field; Gradients

Introduction

Measuring magnetic gradient field anomalies have been used to map regions of differing crustal magnetization, both induced and remanent. To record the gradients over large segments of Europe and particularly the Kursh Magnetic Anomaly (KMA) satellite data are essential. Ten years of the CHAMP mission are used in this study but the more recent three satellite Swarm mission, launched in November 2013 will be able to determine the field gradients directly. Our study should be considered as a base line from which Swarm and future mission will serve as a reference.

Source of the Kursk Magnetic Anomaly

The exploitation of iron deposits is of a great economic importance. The Kursk Magnetic Anomaly is located 400 km south of Moscow it is one of the largest magnetic anomaly on Earth. The Proterozoic iron ore deposits are located in a NNW-SSE oriented complex syncline which is superimposed on the Voronezh Bulge anteclise. The Voronezh Bulge is bordered by the Ryazan-Saratov and Pripyat-Dnieper-Donetsk aulacogens Shchipansky and Bogdanova [1]. The extent of the anomaly is approximately 190,000 km^2 and its crustal depth is between 0.5 - 3.0 km. According to Heiland [2] the anomaly was discovered by Smirnov in 1874. The discussion of the anomaly is described by the early works of Lasareff [3], Haalck [4] and more recent investigations by Lapina [5], Taylor and Frawley [6], and Rotanova [7]. Due to its extent and large magnetization it can be detected by satellite measurements (Magsat, Taylor and Frawley 1987; The resultant magnetization is 3 Am^{-1} (Taylor and Frawley [6]. Our inversion computations are based on their value. The direction of the resultant magnetization is 47° East declination 67° down inclination. The Kursk magnetic anomaly was computed 324 km altitude from CHAMP measurements Figure 1 Kis et al. [8].

Development of the Iron-Ore Deposits

The texture of iron ore bodies can be banded iron formation (BIF) and/or granular iron formation (GIF), Bekker et al. [9]. These marine sediments were formed in the Archean and Paleoproterozoic. Their maximum age is 2.6 *ca*. Ga. The BIF were dominant in the Archean and

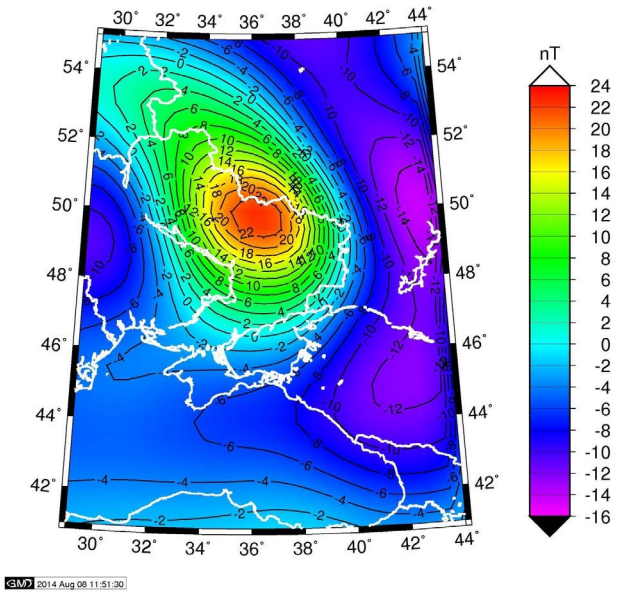

Figure 1: Kursk total magnetic anomaly map computed from CHAMP satellite data at 324 km altitude and plotted in an Albers Equal area conic projection. C. I.=2 nT.

***Corresponding author:** Taylor PT, Planetary Geodynamics Laboratory, NASA/GSFC, Greenbelt, MD 20771, USA, Tel: +1-650-268-9744; E-mail: patrick.t.taylor@nasa.gov

Received June 09, 2016; **Accepted** June 29, 2016; **Published** June 31, 2016

Citation: Kis KI, Taylor PT, Wittmann G (2016) Determination of the Earth's Magnetic Field Gradients from Satellites Measurements and Their Inversion over the Kursk Magnetic Anomaly. J Aeronaut Aerospace Eng 5: 164. doi:10.4172/2168-9792.1000164

earliest Paleoproterozoic while GIF were in the later Paleoproterozoic. A summary of these geological processes which formed the Kursk iron-ore structures are given in Voskresenskaya [10], Alexandrov [11], Shchipansky and Bogdanova [1], Bekker et al. [9], Kovács and Pálfy [12].

These deposits contain considerable qualities of iron in siliceous banded structures. One theory is that the iron originated from marine and submarine volcanic activities or the possible from mantle plumes near the sea bottom. The precipitation of iron depends on the redox conditions of the environment, since the reduced Fe (II) remains as a liquid while the oxide Fe (III) precipitates in anoxic setting. The formation of iron deposits was prevented by the Great Oxidation Event ca. 2.4 Ga. The reductive environment of the hydrosphere ended and the oxygen content increased. This event was due to the decline of volcanic activities. The production of BIF's may have reached a maximum at *ca* 1.85 Ga, since the magmatic activity was greater at this time. The composition of BIFs and GIFs indicates that it is probably of submarine origin.

Three possible oxidative processes are summarized by Bekker et al. [9]. The first description: the origin of the oxygen is from a photosynthetic process of cyanobacteria in a thin oxidative zone in the upper layer of the sea.. Under this layer there are some anoxic water columns where Fe (III) precipitates. According to the second version the iron oxidizing bacteria live in an anoxic environment. These proto-bacteria are able to absorb water and carbon dioxide. The third process: ultraviolet photons oxidize the Fe (II) liquid to Fe (III) solids. Bekker et al. [9] state that the third process is less probable.

Determining CHAMP Magnetic Anomaly Gradients

The gradients of the magnetic field can be either determined directly from the two side by side lower orbiting SWARM satellites. The gradients of the magnetic field can also be computed from the CHAMP anomalies.

Previously we Taylor et al. [13] calculated the horizontal gradients over the Kursk magnetic anomaly. In this study the vertical, north and east gradients will be computed.

CHAMP magnetic anomalies over the European region and the KMA were calculated at 324 km altitude. These anomalies are plotted in a spherical polar coordinate system Kis et al. [8] (Figure 2).

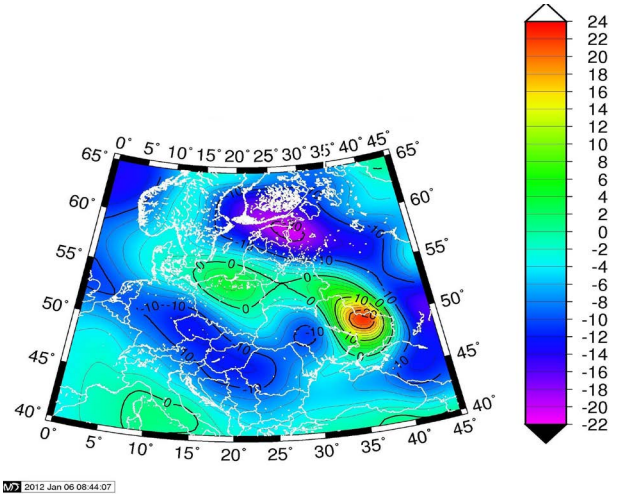

Figure 2: Total magnetic anomaly map over part of Europe at 324 km. C. I.= 2nT.

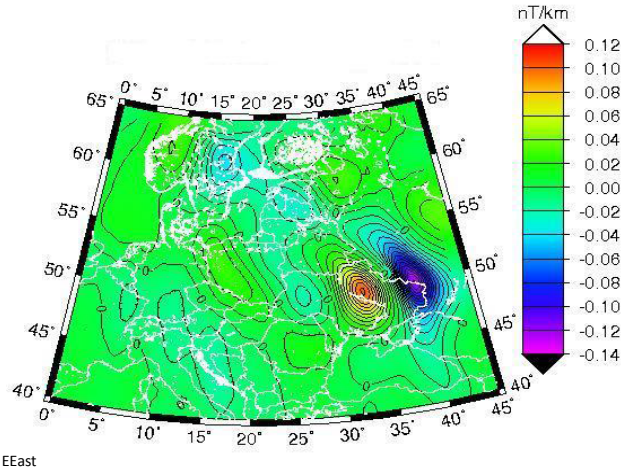

Figure 3: East gradient contour interval is 0.2 nT/km spherical distance is 1 degree.

The numerical horizontal gradients are calculated (from the anomaly data plotted in Figure 2) when the data are in the same latitude but different longitude (the longitude distances will be 1, 2, and 4 degrees, respectively). The spherical distance Δ between two data values is given by the spherical triangle cosine theorem:

$$\cos\Delta = \cos\vartheta\cos\vartheta + \sin\vartheta\sin\vartheta\cos(\lambda_2 - \lambda_1) \quad (1)$$

Where $_{d=R\cos^{-1}}$ is the polar distance, λ_2 and λ_1 are the two longitudes, respectively. The distance of these two data is given by the equation:

$$d = R\cos^{-1}\Delta \quad (2)$$

Where R is the Earth's spherical radius, 6371.2 km + 324 km. The Eastern gradients are approximated by the simple equation of

$$\frac{T(R,\vartheta,\lambda_2) - T(R,\vartheta,\lambda_1)}{d} \quad (3)$$

where T indicates the total magnetic anomaly. The East gradients determined by this method are shown in Figs. 3, 4 and 5. The longitude distance, λ_2-λ_1 was 1° the East gradients are shown in Figure 3. In this case the d distance varies between 88.86 and 49.75 km due to the meridional convergence. The longitudinal distance is 2° in Figure 4, and distance d is between 177.71 and 99.51 km, while the distance d is changed between 355.42 and 199.02 km. It can be seen from Figures 3-5 that the appropriate spherical distances will be 1° or 2° for the gradient determination for the SWARM anomalies.

The second method for computing the gradients is based on the application of the transfer and weight functions of the x-, y- and z- axes Kis and Puszta, [14]. The transfer functions of the above mentioned gradients are given by Blakely [15]:

$$S_{dx}(f_x,f_y) = j2\pi f_x, \quad S_{dy}(f_x,f_y) = j2\pi f_y, \quad S_{dz}(f_x,f_y) = 2\pi\left(f_x^2 + f_y^2\right)^{1/2} \quad (4)$$

Where S_{dx}, S_{dy} and S_{dz} are the transfer functions of the x-, y- and z- gradients; f_x and f_y are the spatial frequencies, j is the imaginary unit. Gaussian low-pass window of:

$$S^W(f_x,f_y) = e^{-k^2\left(f_x^2+f_y^2\right)} \quad (5)$$

Is applied for the above mentioned transfer functions, where k is the appropriate parameter of the windowed transfer functions. The weight functions of the windowed transfer functions are:

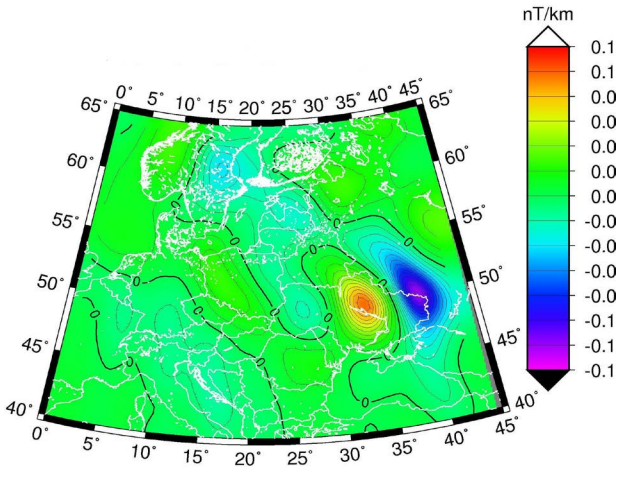

Figure 4: East gradient of European total magnetic anomalies (figure 2) at 324 km altitude (Albers projection) Spherical distance is 2 degrees.

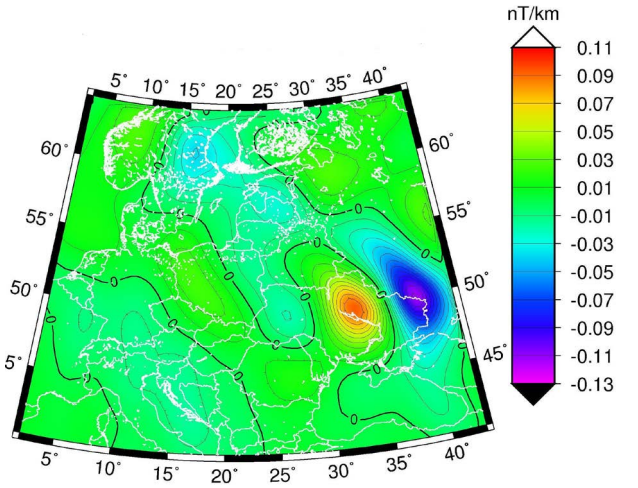

Figure 5: East Gradient of European total magnetic anomalies (Figure 2) spherical distance is 4 degrees.

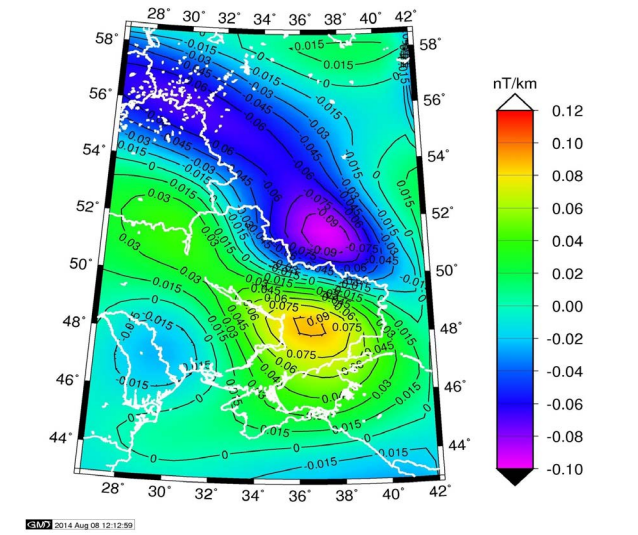

Figure 6: North gradient of KMA (Fig. 1 on an Albers' projection). C.I.=0.015nT/km.

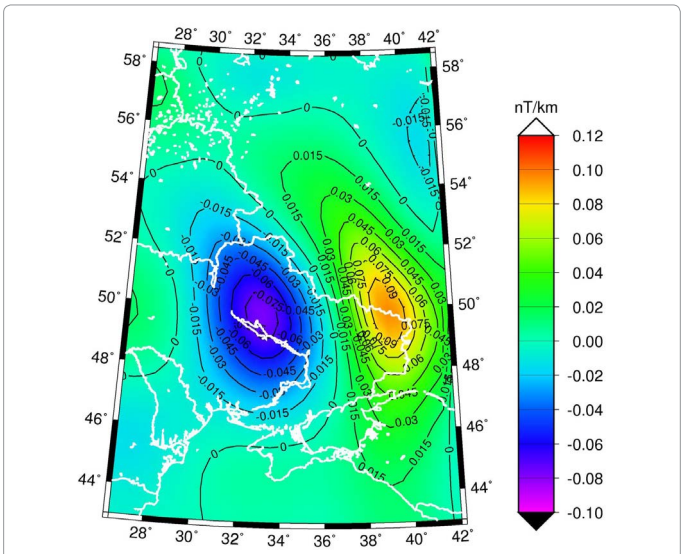

Figure 7: East gradient of KMA (Fig. 1) in Albers' projection. C. I.=0.015nT/km .

$$S_{dx}^{w}(x,y) = -\frac{2\pi^2}{k^4} x\, e^{-\frac{\pi^2}{k^2}\left(x^2+y^2\right)} \tag{6}$$

$$S_{dy}^{w}(x,y) = -\frac{2\pi^2}{k^4} y\, e^{-\frac{\pi^2}{k^2}\left(x^2+y^2\right)} \tag{7}$$

$$S_{dz}^{w}(x,y) = \frac{\pi^{5/2}}{k^3} e^{-\frac{\pi^2}{k^2}\left(x^2+y^2\right)} M\left(-\frac{1}{2},1,\frac{\pi^2\left(x^2+y^2\right)}{k^2}\right) \tag{8}$$

Where M is the confluent hypergeometric function (Slater, 1976). The development of the (6) – (8) functions is given by Kis and Puszta [14].

If the gradients are computed by the above method than the CHAMP anomalies should be transformed from the spherical polar coordinate system to the Cartesian coordinate system. The zero of the Descartes coordinate system is placed at an altitude of 324 km and at latitude 48.75° and longitude 36.25°. The transformation is given by Kis et al. [16]. The windowed gradients are computed in the Cartesian coordinate system and the next step is their transformation into the spherical polar coordinate system. These gradients are shown in the Figures 6-8 in an Albers' projection. These gradients emphasize the depth variation or change in magnetization of the source or both. These results are not determined unambiguously from the gradients. The gradients in Fig. 6 show the Northeast- Southwest elongation of the Kursk anomalies while Fig. 7 illustrates the East-West variation. The vertical gradient, Figure 8 displays a Northwest-Southeast directional asymmetry.

The third method for calculating the vertical gradient is using the Hilbert transform. The Hilbert transform was named by G. H. Hardy (1932), the English mathematician, out of deference to D. Hilbert, the German mathematician. Nabighian [17,18] Nabighian and Hansen [19] Guspi and Novara [20] applied Hilbert transforms to the analysis of potential fields.

Let us consider the equation:

$$F\left\{\frac{\partial T}{\partial z}\right\} = -\frac{jf_x}{\left(f_x^2+f_y^2\right)^{1/2}} F\left\{\frac{\partial T}{\partial x}\right\} - \frac{jf_y}{\left(f_x^2+f_y^2\right)^{1/2}} F\left\{\frac{\partial T}{\partial y}\right\} \tag{9}$$

Given by Nabighian [18], where F is the Fourier transform. This equation can be expressed in a simpler form:

Where H_1 and H_2 are the Hilbert transform, that is:

$$F\left\{\frac{\partial T}{\partial z}\right\} = H_1 F\left\{\frac{\partial T}{\partial x}\right\} + H_2 F\left\{\frac{\partial T}{\partial y}\right\} \tag{10}$$

$$H_1 = -\frac{jf_x}{\left(f_x^2 + f_y^2\right)^{1/2}} \quad \text{and} \quad H_2 = -\frac{jf_y}{\left(f_x^2 + f_y^2\right)^{1/2}} \tag{11}$$

The inverse Fourier transform of Equation (9) is:

$$F^{-1}\left\{\frac{-jf_x}{\left(f_x^2 + f_y^2\right)^{1/2}}\right\} = \frac{1}{2\pi}\frac{x}{\left(x^2 + y^2\right)^{3/2}} \tag{12}$$

and

$$F^{-1}\left\{\frac{-jf_y}{\left(f_x^2 + f_y^2\right)^{1/2}}\right\} = \frac{1}{2\pi}\frac{y}{\left(x^2 + y^2\right)^{3/2}} \tag{13}$$

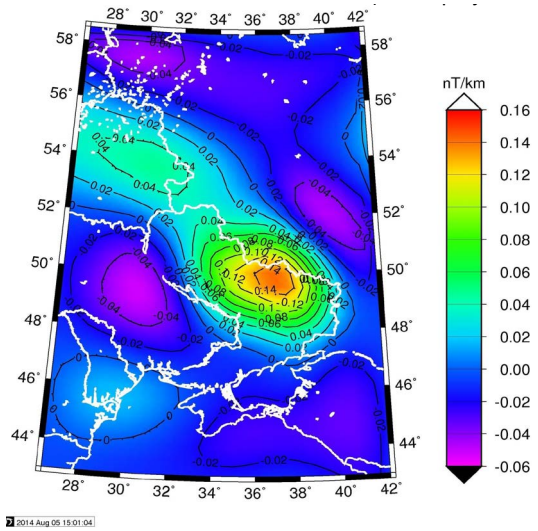

Figure 8: Vertical gradient of KMA (Figure 1.) C.I.=0.02 nT/km.

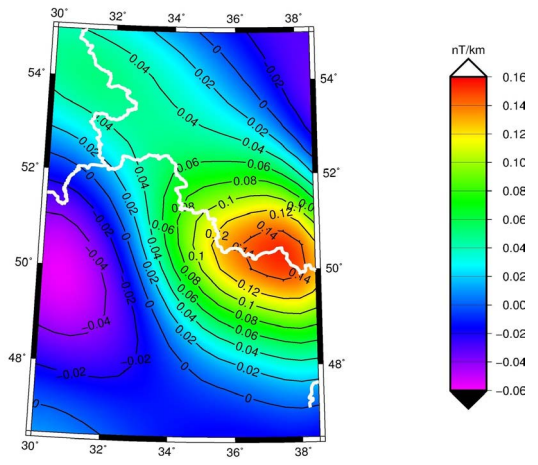

Figure 9: Vertical gradient of KMA (Figure 1) computed by Hilbert transform, C.II=0.02nT/km.

These inverse Fourier transforms are given by Nabighian [18] in his Appendix A. The CHAMP magnetic anomaly field (Fig. 1) is transformed from the spherical polar coordinate system to the Descartes coordinate system. Now the Hilbert transform is computed in the spherical polar coordinate system and the vertical gradients given in Figures 8 and 9, they illustrate virtually the same results.

Inversion of the Kursk Magnetic Anomaly

The Bayesian inference was applied to the inversion of the Kursk Magnetic Anomaly. The Bayesian inference is widely used in the inversion procedures and is summarized by Box and Tiao [21,22], Tarantola [23], Duijndam [23,24], Menke [25], Gregory [26], Kis et al. [16] and Kis et al. [8].

The Kursk Magnetic Anomaly are shown in the spherical polar coordinate system (Figures 10-13). The inversion procedure is applied in the Descartes coordinate system so the earlier mentioned transformation should be used. The result is given in the Descartes coordinate system that was computed from the CHAMP data.

The forward model from the inversion is a quadrangle with horizontal upper and lower levels we computed the anomaly using Plouff's [27] method. This is an idealized model of the Kursk source [28-33]. We used 3 Am^{-1} average magnetization given by Taylor and Frawley [6] and the average direction of magnetization inclination 47°down and 67°East declination given by Bhattacharyya.

The basic equation of the Bayesian inference is:

$$p(\mathbf{m}\,|\,\mathbf{d}) = p(\mathbf{d}\,|\,\mathbf{m})\,p(\mathbf{m}), \tag{14}$$

Where p ($\mathbf{m}|\mathbf{d}$) is the $p^{a\ posteriori}$ conditional probability density, p ($\mathbf{d}|\mathbf{m}$) is the *likelihood* conditional probability density, $p(\mathbf{m})$ is the *pa priori* probability density. The vector $\mathbf{m}$ is the estimated parameters of the forward model and the vector $\mathbf{d}$ the measured CHAMP magnetic anomalies. The $p^{a\ \text{posteriori}}$ conditional probability density for Gaussian multivariate distribution can be expressed in the following form:

$$p^{a\ posteriori} \propto exp\left(-\frac{1}{2}\left(\mathbf{m}-\mathbf{m}^{a\ priori}\right)^T \mathbf{C}_m^{-1}\left(\mathbf{m}-\mathbf{m}^{a\ priori}\right)\right) \\ exp\left(-\frac{1}{2}\left(\mathbf{d}^{measured}(x,y)-\mathbf{T}^{calculated}(x,y,\mathbf{m})\right)^T \mathbf{C}_D^{-1}\left(\mathbf{d}^{measured}(x,y)-\mathbf{T}^{calculated}(x,y,\mathbf{m})\right)\right), \tag{15}$$

where vector $\mathbf{m}^{a\ priory}$ is the parameters estimated by the interpreter, $\mathbf{C}_m$ is the covariance matrix of the estimated parameters, vector $\mathbf{d}^{measured}$ is the measured CHAMP anomalies, $\mathbf{T}^{calculated}$ $(x,y,\mathbf{m})$ is the calculated values at the coordinate (x,y), calculated for the $\mathbf{m}$ parameters, $\mathbf{C}_D$ is the covariance matrix of the CHAMP measured anomalies, superscript T the transposed vector.

The $p^{a\ \text{posteriori}}$ conditional probability density for a Laplacian distribution is:

$$p^{a\ posteriori} \propto exp\left(-\frac{\left|\mathbf{m}-\mathbf{m}^{a\ priori}\right|}{\mathbf{C}_m^{\frac{1}{2}}}\right) exp\left(-\frac{\left|\mathbf{d}^{measured}(x,y)-\mathbf{T}^{calculated}(x,y,\mathbf{m})\right|}{\mathbf{C}_D^{\frac{1}{2}}}\right). \tag{16}$$

We want to maximize the p^a *posteriori* probability density given by the equations (15) and (16) as a function of the parameter $\mathbf{m}$. This is equivalent to minimizing the sum of exponent of the equations (15) and (16). The functions $E(\mathbf{m})$ which will be minimized for multivariate Gaussian parameter distribution are:

$$E(\mathbf{m}) = (\mathbf{m}-\mathbf{m}^{a\ priori})^T \mathbf{C}_m^{-1}\left(\mathbf{m}-\mathbf{m}^{a\ priori}\right) + (\mathbf{d}^{measured}(x,y) \\ -\mathbf{T}^{calculated}(x,y,\mathbf{m}))^T \mathbf{C}_D^{-1}\left(\mathbf{d}^{measured}(x,y)-\mathbf{T}^{calculated}(x,y,\mathbf{m})\right) \tag{17}$$

For the multivariate Laplacian parameter distribution:

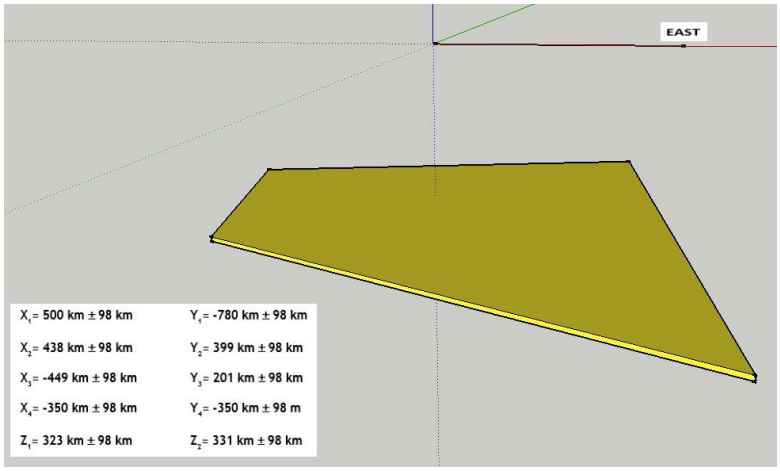

Figure 10: Computed model in Cartesian coordinates data have a Gaussian distribution with the minimum problem being solved using the simplex method. The table shows the determined parameter values and their maximum error.

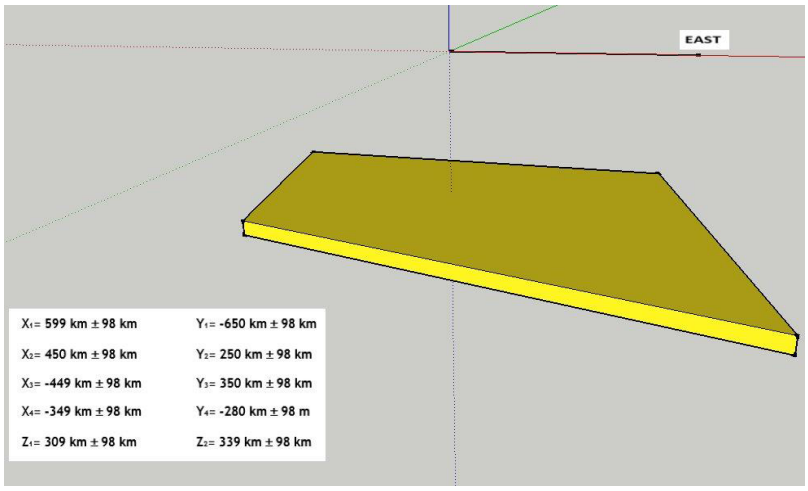

Figure 11: Computed model in Cartesian coordinates, the data have Gaussian distribution with the minimum problem being solved using the simulated annealing method. Table shows the calculated parameter values and their maximum error.

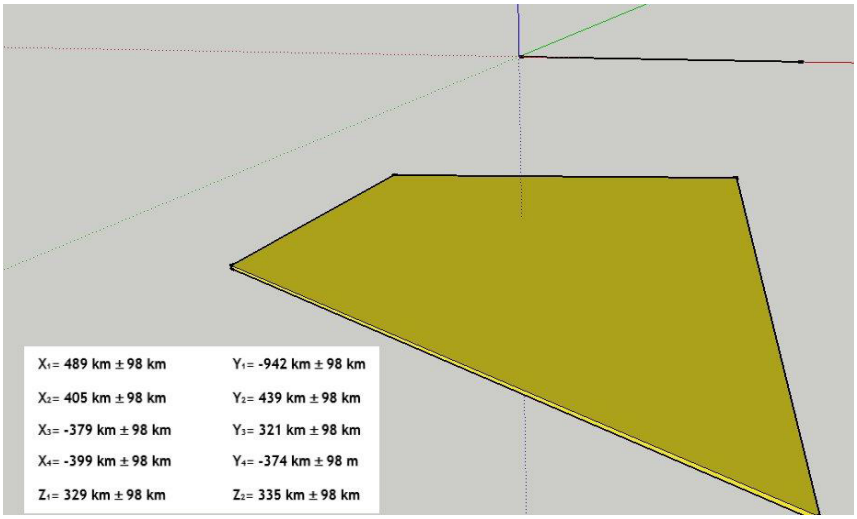

Figure 12: Computed model in Cartesian coordinates, , the data have a Laplace distribution with the minimum problem being solved by the simplex method. The results are given in tabular form with the determined parameter values and their maximum error.

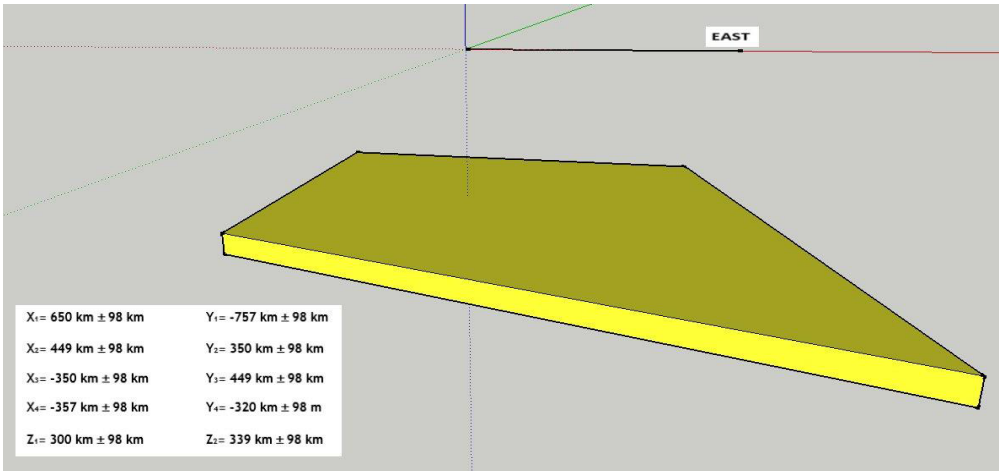

Figure 13: Computed model in Cartesian coordinates, the data have a Laplace distribution with the minimum problem being solved by simulated annealing method. The tale in the figure show the calculated parameter values and their maximu, error.

	Parameter	Gaussian distribution model parameter	Laplacian distribution model parameter
simplex method	x_1	500 km ± 98 km	489 km ± 98 km
	x_2	438 km ± 98 km	405 km ± 98 km
	x_3	-449 km ± 98 km	-379 km ± 98 km
	x_4	-350 km ± 98 km	-399 km ± 98 km
	y_1	-780 km ± 98 km	-942 km ± 98 km
	y_2	399 km ± 98 km	439 km ± 98 km
	y_3	201 km ± 98 km	321 km ± 98 km
	y_4	-350 km ± 98 km	-374 km ± 98 km
	z_1	323 km ± 98 km	329 km ± 98 km
	z_2	331 km ± 98 km	335 km ± 98 km
simulated annealing method	x_1	599 km ± 98 km	650 km ± 98 km
	x_2	450 km ± 98 km	449 km ± 98 km
	x_3	-449 km ± 98 km	-350 km ± 98 km
	x_4	-349 km ± 98 km	-357 km ± 98 km
	y_1	-650 km ± 98 km	-757 km ± 98 km
	y_2	250 km ± 98 km	350 km ± 98 km
	y_3	350 km ± 98 km	449 km ± 98 km
	y_4	-280 km ± 98 km	-320 km ± 98 km
	z_1	309 km ± 98 km	300 km ± 98 km
	z_2	339 km ± 98 km	339 km ± 98 km

Table 1: Computed models in Cartesian coordinates, the data have Gaussian and Laplace distributions. The optimum problems are solved by simplex and simulated annealing methods.

$$E(\mathbf{m}) = \frac{\left|\mathbf{m}-\mathbf{m}^{a\ priori}\right|}{\mathbf{C}_{\mathbf{m}}^{1/2}} + \frac{\left|\mathbf{d}^{mért}(x,y)-\mathbf{T}^{számított}(x,y,\mathbf{m})\right|}{\mathbf{C}_{\mathbf{D}}^{1/2}}. \quad (18)$$

The $E(\mathbf{m})$ functions equations (17) and (18) will be minimized using the regularization suggested by Tikhonov and Arsenin (1977) is:

$$E(\mathbf{m}) = (\mathbf{m}-\mathbf{m}^{a\ priori})^T \mathbf{C}_m^{-1}\left(\mathbf{m}-\mathbf{m}^{a\ priori}\right) + (\mathbf{d}^{measured}(x,y) - \mathbf{T}^{calculated}(x,y,\mathbf{m}))^T \mathbf{C}_D^{-1}\left(\mathbf{d}^{measured}(x,y)-\mathbf{T}^{calculated}(x,y,\mathbf{m})\right)+\lambda(\mathbf{m}_{i+1}-\mathbf{m}_i)^2 \quad (19)$$

and

$$E(\mathbf{m}) = e^{\frac{\left|\mathbf{m}-\mathbf{m}^{a\ priori}\right|}{\mathbf{C}_{\mathbf{m}}^{1/2}}} + \frac{\left|\mathbf{d}^{mért}(x,y)-\mathbf{T}^{számított}(x,y,\mathbf{m})\right|}{\mathbf{C}_{\mathbf{D}}^{1/2}} + \left|\mathbf{m}_{i+1}-\mathbf{m}_i\right| \quad (20)$$

Where λ is the regularization parameter. According to the earlier investigations Kis et al. [8] the appropriate value of λ is between 1 – 10.

The minimum problem is solved by the simplex Walsh [28] and simulated annealing Kirkpatrick et al. [29] methods. In the present investigation the *a priori* covariance matrix is a diagonal one whose variances is 10 km^2, the *likelihood* covariance matrix is also diagonal one whose variances is 2 nT^2. The determined models are visualized in the model values are presented in Table 1 for the Descartes coordinate system. The maximum errors are determined by the model parameter errors.

Conclusion

The three methods for the determination of the gradients of the satellite magnetic anomaly data (at an altitude of 324 km) over the KMA are presented in spherical polar coordinates. All of them resolve the anomalies and they show the complex structure of its source. Both the windowed vertical gradient and the vertical gradient by the Hilbert transform give very similar results. All of the gradient methods can be applied. Three inversions (for Gauss distribution and the parameters determined by the simplex method; Gaussian distribution and the parameters determined by simulated annealing method; Laplacian distribution and the parameters determined by simulated annealing method) give comparable result within their maximum errors.

References

1. Shchipansky AA, Bogdanova SV (1996) The Sarmatian crustal segment precambrian correlation between Voronezh Massif and the Ukraine shield across the Dnieper-Donetsk aulacogen. Tectonophysics 286: 109-125.
2. Heiland CA (1946) Geophysical exploration. Prentice Hall Company.
3. Lasareff P (1923) The anomalies of terrestrial magnetism and gravity in the Kursk Government, Russia. Terrestrial Magnetism: 123-124.
4. Haalck H (1929) Zur Frage der Erklärung der Kursker magnetischen und gravimetrischen Anomalie. Gerlands Beiträge zur Geophysik 22: 241-255.
5. Lapina MI (1960) On certain results obtained from the study of vertical gradients of a magnetic field in the area of the Kursk magnetic anomaly. Bulletin Academy of Sciences USSR Geophysics Series: 390-395.
6. Taylor PT, Frawley JJ (1987) Magsat anomaly data over the Kursk region USSR Physics of the Earth and Planetary Interiors 45: 275-265.
7. Rotanova NM, Kharitonov AL, Frunze AKH, Filippov SV, Abramova D (2005) Anomalous magnetic fields measured on the CHAMP satellite for the territory of the Kursk Magnetic anomaly. Geomagnetism and Aeronomy 45: 671-678.
8. Kis KI, Taylor PT, Wittmann G, Toronyi B, Puszta S (2012) Interpretation of the total magnetic field anomalies measured by the CHAMP satellite over a part of

Europe and the Pannonian basin. Acta Geodaetica et Geophysica Hungarica 47: 130-140.

9. Bekker A, Slack JF, Planavsky N, Krapez B, Hofmann A et al. (2010) Iron formation the sedimentary product of a complex interplay among mantle tectonic oceanic and biospheric processes. Economic Geology 105: 467-508.
10. Voskresenskaya MN (1965) Relations between Archean and Proterozoic rocks in Kursk magnetic anomaly. International Geology Review 11: 454-460.
11. Alexandrov EA (1973) The Precambrian banded iron formations of the Soviet Union. Economic Geology 68: 1035-1062.
12. Kovács Zs, Pálfy J (2014) A rozsdamentes Föld talányos bányakincse. Természet Világa 145: 156-160.
13. Taylor PT, Kis KI, Wittmann G (2014) Satellite-altitude horizontal magnetic gradient anomalies used to define the Kursk magnetic anomaly. J Applied Geophysics 109: 133-139.
14. Kis KI, Puszta S (2006) Application of field derivatives for locating Sarmatian graves. J Applied Geophysics 60: 13-26.
15. Blakely R (1995) Potential theory in gravity and magnetic applications. Cambridge University Press.
16. Kis KI, Taylor PT, Wittmann G, Toronyi B, Puszta S (2011) Inversion of magnetic measurements of the CHAMP satellite over the Pannonian Basin. J Applied Geophysics 75: 412-418.
17. Nabighian MN (1972) The analytical signal of two-dimensional magnetic bodies with polygonal cross-section: its properties and use for automated anomaly interpretation. Geophysics 37: 507-517.
18. Nabighian MN (1984) Towards a three-dimensional automatic interpretation of potential field data via generalized Hilbert transform: Fundamental relations. Geophysics 49: 780-786
19. Nabighian MN, Hansen RO (2001) Unification of euler and werner deconvolution in three dimensions via generalized Hilbert transform. Geophysics 66: 1805-1810.
20. Guspi F, Novara I (2012) Generalized Hilbert transforms of the effect of single magnetic sources. Geophysics 77: J7-J14.
21. Box GEP, Tiao GC (1973) Bayesian inference in statistical analysis. Addison-Wesley.
22. Tarantola A (1987) Inverse problem theory methods for data fitting and model parameter estimation. Elsevier Amsterdam, Oxford -New York -Tokyo.
23. Duijndam AJW (1988a) Bayesian estimation in seismic inversion Part I: Principles. Geophysical Prospecting 36: 878-898.
24. Duijndam AJW (1988b) Bayesian estimation in seismic inversion Part II: Uncertainty Analysis. Geophysical Prospecting 36: 899-918
25. Menke W (1989) Geophysical data analysis: Discrete inverse theory. Elsevier Inc., Academic Press, San Diego-New York-Boston-Sydney-Tokyo-Toronto.
26. Gregory PC (2005) Bayesian logical data analysis for the physical sciences. Cambridge University Press.
27. Plouff D (1976) Gravity and magnetic fields of polygonal prisms and application to magnetic terrain correction. Geophysics 41: 727-741.
28. Walsh GR (1975) Methods of optimization. John Wiley & Sons, London.
29. Kirkpatrick S, Gelatt Jr CD, Vecchi NP (1983) Optimization by simulated annealing. Science 220: 671-680.
30. Bhattacharayya BK (1980) A generalized multi-body model for inversion of magnetic anomalies. Geophysics 45: 255-270.
31. Hardy GH (1932) On Hilbert transforms. Quart J Math (Oxford) 3: 102-112.
32. Slater LJ (1970) Confluent hypergeometric functions. In: Abramowitz M, Stegun IA, (eds.) Szerk Handbook of mathematical functions with formulas, graphs and mathematical tables. US Department of Commerce, National Bureau of Standards Applied Mathematics. Series 55: 503-535.
33. Tikhonov AN, Arsenin VY (1977) Solutions of ill-posed problems. John Wiley & Sons, New York-Toronto-London-Sydney.